Journal of
Nanoscience and Nanotechnology
Vol. 11, 9136–9142, 2011

Nanostructure and Internal Strain Distribution in Porous Silicon

Mihaela Miu*, Mihai Danila, Irina Kleps, Adina Bragaru, and Monica Simion

National Institute for Research and Development in Microtechnologies (IMT-Bucharest),
Erou Iancu Nicolae str. 126A, 077190, Bucharest, Romania

Porous silicon (PS) layers with different degrees of porosity have been fabricated and their nanostructure has been investigated using complementary methods as FE–SEM (field emission scanning electron microscopy), SAXS (small-angle X-ray scattering), and Raman spectroscopy. Correlation of these results with strain analyses is also required for envisaged applications in MEMS technology. Symmetrical and asymmetrical rocking curves obtained by high-resolution X-ray diffraction completed with reciprocal space maps (RSMs) explain the features observed in Raman spectra: the PS film in-depth contains two layers—bulk and highly strained superficial layer, between them being a graded strain layer.

Keywords: Nanostructured Material, Porous Silicon, Strain, Raman Spectroscopy, Triple-Axis X-ray Diffraction.

1. INTRODUCTION

The analyses performed on porous silicon (PS) reveal that this material exhibits necessary properties for a broad area of mechanical, thermal, electrical or optical applications; furthermore, the high internal surface area allows happening of chemical interactions and subsequently efficient functionalisations.[1,2] All these performances make the PS layers widely used in micro-electro-mechanical systems (MEMS) fabrication.[3,4] The recent developments, which imply requirements in both decreasing of dimensions and improvement of reliability and sensibility of devices, make necessary the control of stress in structures, and consequent understanding of its origin. The intrinsic stress, as well as the stress introduced into films and/or structures during processing and storage have to be taken into consideration[5] and in this view, the porous silicon layer analysis implies correlation of the nanostructure, internal strain and chemical composition.

Taking into account the previously reported results in this area,[6–8] advanced methods have been used to obtain new and accurate information: field emission scanning electron microscopy, triple-axis rotating anode X-ray diffraction, and high resolution Raman spectroscopy. While microscopic technique presents rather the local properties of material, the other ones provide information about the structure of bulk material. Putting all these results together allows a fundamental understanding of PS formation mechanism and consequently a better control of its microstructure for envisaged applications.

2. EXPERIMENTAL DETAILS

A series of PS samples were prepared using a highly doped p^+ type Si substrate (1–5 $m\Omega \cdot cm$)—provided by *Si-Mat* Silicon Materials, Germany; the anodisation process was performed in the AMMT cell for 4 inch wafers, using 25% HF concentration in ethanolic electrolyte solution, at different current densities—10 mA/cm^2, 20 mA/cm^2 and respectively 40 mA/cm^2—preserving constant the process time—10 minutes. After porosification process, the Si wafers have been diced to form 1×1 cm^2 samples, labeled from X1 to X3.

Morphological characterizations were realized using *Nova NanoSEM 630 system*, a Field Emission Scanning Electron Microscope (FE-SEM)—FEI Company, USA—with ultra-high resolution at high and low voltage in high vacuum: 1.6 nm@1 kV.

Raman spectroscopy is a non-destructive technique for structural analysis, the measurements being carried out on High Resolution Raman Spectrometer, *LabRAM HR* 800—Horiba Jobin Yvon—with spectral resolution 0.35 cm^{-1}/pixel and diffraction gratings of 1800 gr/mm. The spectrometer is equipped with a microscope and, the 50× objective was used to focus the incident laser beam

---

*Author to whom correspondence should be addressed.

1533-4880/2011/11/9136/007 doi:10.1166/jnn.2011.4305

to a spot size of about 2 microns on the sample surface and to record the scattered light from a very small focus area. The data were taken at room temperature using the 514.5 nm line of an argon-ion laser (2.4 eV), corresponding a penetration depth around 100 nm.

The crystalline structure of the experimental samples was investigated by different X-ray diffraction (XRD) methods using a *Rigaku Smartlab* thin film triple-axis 9 kW rotating anode diffraction system, equipped with an in-plane arm in θ–2θ angular scanning configuration using a Cu X-ray tube and a multilayer mirror (parallel beam, Cu K_α X-ray wavelength of $\lambda_{K_{\alpha_1}} = 1.540609$ Å), Ge(220) 4 bounce monochromator and a Ge(220) 2 bounce analyzer. The triple axis mode has the advantage of being able to distinguish between strain induced lattice mismatch (revealed by θ–2θ scans) and layer tilt or misorientation (revealed by rocking curves), something that the double-axis XRD technique used in the majority of previous investigations is unable to do.[9] This mode was also used for the measurement of the reciprocal space mapping (RSM) in both symmetric and asymmetric configuration.

3. RESULTS AND DISCUSSION

3.1. Morphological Analyses

The first evidence of porous structure has been obtained using the FE-SEM analyses, and the corresponding cross-section images taken at 45° sample tilt are presented in Figure 1, containing both the general view of the layers and the details of the pores. The pore dimensions taking values according to the etching conditions, e.g., ~5 nm (X1), ~7 nm (X2) and respectively ~9 nm (X3) have been evidenced on figures. The size distribution depends also on the current densities, and while for low and intermediate values the diameters are almost similar, bigger value leads to a relatively broad range of dimensions from 8.5 nm to 10 nm. Moreover, although the process time is equal, the thickness of porous layers is different, as might be observed in the SEM images, higher density of current leading to a corresponding increase of the etching rate; the values summarized in Table I, where the layer thickness was calculated taking into the sample tilt using the formula $L_{\text{PS}} = L_{\text{SEM image}} \cos 45°$.

3.2. Raman Spectroscopy

Raman spectroscopy measurements have been performed to analyze the lattice vibrations and their adjustment induced by porosification process of Si substrate, both being sensitive to composition and crystal quality—the changes of atomic spacing giving information about the strain. In Figure 2 there are presented the Raman spectra recorded for experimental layers in comparison with Si substrate.

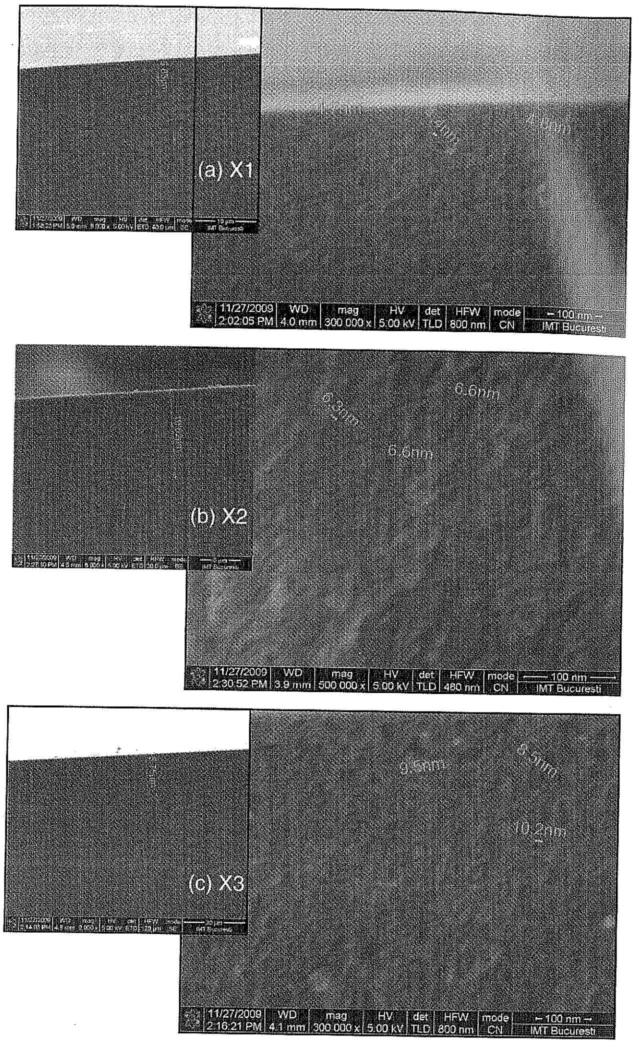

Fig. 1. High-resolution SEM images of the experimental PS layers (labeled X1–X3)—viewing at a tilt angle of ~45°.

The spectra contain scattering peaks corresponding to Si phonon modes; although the crystalline Si(100) has been used as substrate, and corresponding to selection rules only LO mode is allowed, the lattice disorder induced by doping and surface roughness lead to their relax and phonon modes specific to amorphous Si arise. The most intense peak (480–530 cm^{-1}) is those originated from optical modes of Si at central point Γ of the Brillouin zone—including like-transverse (TO) and longitudinal (LO) optical

Table I. Nanostructure of PS layers.

	SEM analyses		Raman analyses			XRD analyses
Samples	Pore size (nm)	PS thickness (μm)	$\omega_{\text{LO-PS}}$ (cm^{-1})	d_{Raman} (nm)	Γ_{PS} (cm^{-1})	d_{SAXS} (nm)
X1	4.7	4	516.82	3.1	9.95	4.2
X2	6.6	7.5	516.04	2.75	12.65	3.7
X3	8.5–10	11	514.68	2.3	17.49	3.32

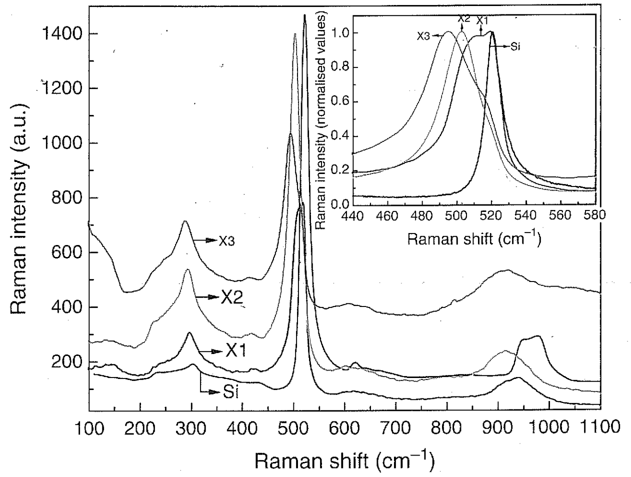

Fig. 2. Raman spectra of PS layers (Xi).

phonons—the rest of them being assigned to transverse (TA)—150 cm^{-1}—and longitudinal (LA)—300 cm^{-1}—acoustic modes, and respectively to the second order TO—930 cm^{-1}– mode.[10]

The insert graph presents the evolution of the main Stokes scattering band allowing a more detailed analysis; comparing with the result for bulk Si–p$^+$(100), it is clear that nanostructuration of substrate leads to a red shifting and an asymmetric broadening due to the phonon confinement effect. The increasing of anodisation current density and consequently the sample porosity lead to the extent of lattice distance expansion, this phenomenon being responsible for the supplementary red shifting of the optical phonon bands observed for the X2 labeled sample and even more for X3.

On the other hand, the asymmetry of the Raman lineshapes is not due to the quantum confinement alone, contributions from inhomogeneous laser heating[11] or from Fano interaction between phonon Raman scattering and electronic Raman scattering involving photo-excited electrons[12] have been demonstrated.

The deconvolution of each Raman spectrum in the range 440–600 cm^{-1} shows that they might be split into three bands: the first one is a broad band with the lowest intensity, at around 480 cm^{-1} being the contribution of the amorphous content from porous layers; the second and the third ones are located in close proximity to each other, at 500 ± 10 cm^{-1} and respectively in the range 515–520 cm^{-1}.

Tsu et al. considered that the origin of the last peaks is the separation of the transversal optical (TO) and longitudinal optical (LO) phonon modes bands.[13] On the other hand, because the hydride terminated freshly etched porous silicon (PS) surface is readily oxidized by simple storage in atmosphere,[14] Pusep et al. assigned the intermediate peak to the new formed interface Si/SiO$_2$, which is considerable strained comparing with the previous one.[15] Given that the Raman spectra recorded for our samples do not have extra-features which can be attributed to the contribution from nano-SiO$_2$ even though SiO$_2$ surrounds the Si nanofibrils,[16] the scattering features observed in the range 500–520 cm^{-1} should have other explanation.

Our approach is to take into consideration the particularity of silicon porosification process, specifically formation during the PS advancement of a superficial layer resulted from the two-step disproportionate reaction of anodisation;[17] the presence of a thin more porous layer might be observed in cross-section SEM images—Figure 2(b). Therefore, the deconvolution of the Si phonon peak in two bands might be attributed to the presence of different size crystallites, more probably coming from the superficial top-layer and bulk-layer, and consequently indicates the variation of internal strain in the film.

An additional process has been utilized to verify the influence of this superficial layer, dipping of the samples into 40% HF for 30 sec., sufficient time to etch it, remaining only bulk PS layer—the sample have been labeled Xi$_e$. In Figure 3 there are presented the reiterated Raman analyses and it could be observed that the peaks previous positioned at about 500 cm^{-1} disappear. Moreover, the intensity of the amorphous phase peak is significantly reduced and it could be neglected. In order to obtain supplementary information about the nature of this top layer and the possibility to control its influence, different X-ray diffraction analyses have been proceeded.

Since the Raman shift of the phonon frequency observed after additional etching is specific for PS bulk-layers, it is possible more accurate determination of characteristic size of crystalline domains. The shift in the wavenumber of the LO Raman phonon between substrate ($\omega_{\mathrm{Si-p^+}}$) and PS (ω_{PS}) has been used to estimate the mean crystallite size, assuming spherical shape, based on the following formula given by the bond polarization model—BPM—which

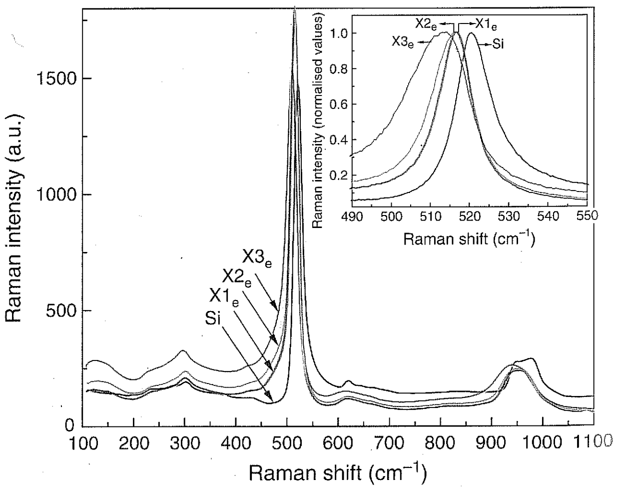

Fig. 3. Raman spectra of PS layers after the additional etching process (Xi$_e$).

takes into account the quantum confinement effects:[18, 19]

$$\Delta\omega = \omega_{PS} - \omega_{Si-p^+} = -\alpha \cdot \left(\frac{a}{d_{Raman}}\right)^{\gamma}$$

where: d_{Raman} is average crystallite diameter, $a = 0.543$ nm is the lattice constant of Si, and α, γ are parameters that take the values $\alpha = 47.41$ cm^{-1}, $\gamma = 1.44$ for spherical crystallites. Moreover, the estimation of d_{Raman} from presented expression ($d_{Raman} = a \cdot (-\Delta\omega/\alpha)^{-1/\gamma}$) has been resolved taking into account the presence of an initial shift in the wavenumber in Si substrate, $\omega_{Si-p^+} = 520.62$ cm^{-1}, compared with the intrinsic (single crystal) characteristic c-Si Raman band at the 521 cm^{-1};[20] the shift is accompanied by a larger linewidth, the corresponding full width at half maximum (FWHM) taking values from ~4 cm^{-1} to 9 cm^{-1}, these features deriving from the highly doping of semiconductor by means of boron impurities.

The average crystallite diameters—d_{Raman}—calculated using the optical phonons peak position indicated after the etching process are 3.1 nm for X1$_e$ sample, and respectively 2.75 nm for X2$_e$ and 2.3 nm for X3$_e$ (Table I). Regarding the Γ_{PS} values, they increase with TO Raman frequencies decrease, and furthermore the mean sizes of Si crystallites have an inverse dependence on the peak width; on the other hand, the broadening of the main Raman peaks might be attributed to structural disorder in the lattice structure.

3.3. X-Ray Diffractometry and Strain Measurements

Besides microscopical and Raman analyses, small-angle X-ray scattering (SAXS) has been applied for complementary investigation of microstructure and morphology for the experimental PS layers, because the measurement is averaged over all sample surface, giving statistical information over several square millimeters at variance to microscopy.[21] SAXS allows measuring the diffuse X-ray scattering induced by pores and surface roughness, and moreover, the grazing incidence reflective SAXS experimental set-up (GI-SAXS) enables us to characterize the pore structure with a good accuracy.[22, 23] The grazing angle of incidence was selected in the range 0.1° $< \alpha <$ 8°. The SAXS spectra have been fitted assuming spherical shapes crystallites and the values are listed in Table I.

It could be observed that the mean dimensions of the Si nanocrystallite estimated from Raman method—d_{Raman}—are smaller than those calculated from XRD technique—d_{SAXS}. The differences could appear due to fact that the scattered light in Raman spectroscopy is recorded from a very small focus area-ca. 2 μm diameter—where it is a limited number of crystallites, the Raman intensity being summarization of intensities contributed by each of them within spot.[24] As a result, the tensile strain effect from nanograin boundaries become significant leading to a supplementary redshift of the phonon peak and consequently to a calculated smaller mean size value.[25]

To investigate the changes in lattice mismatch/strain with current density, combining rotation ω of the sample and rotation 2θ of the analyzer, the $\omega/2\theta$ scans were performed on the (004) plane, this technique being very sensitive to lattice displacement in the direction perpendicular to the diffraction plane of the crystal. High-resolution triple axis X-ray diffraction was used to obtain symmetrical and asymmetrical rocking curves and the HRXRD data acquired from experimental samples are presented in Figure 4.

Regarding the XRD spectra deconvolution and consequently finding the real peak positions for Si, PS$_{surf}$ and PS$_{bulk}$, as they are presented in Table II, it has to be mentioned that the incident beam is highly monochromatic and fulfill the plane wave approximation. *In this experimental set-up the peak positions and resulting interplanar distances (lattice spacings) are the absolute ones*, with basically no influence of instrumental errors [alignment being an automatic procedure, tilt and miscut angles are compensated by manual alignment with respect to the atomic plane Si(004)].

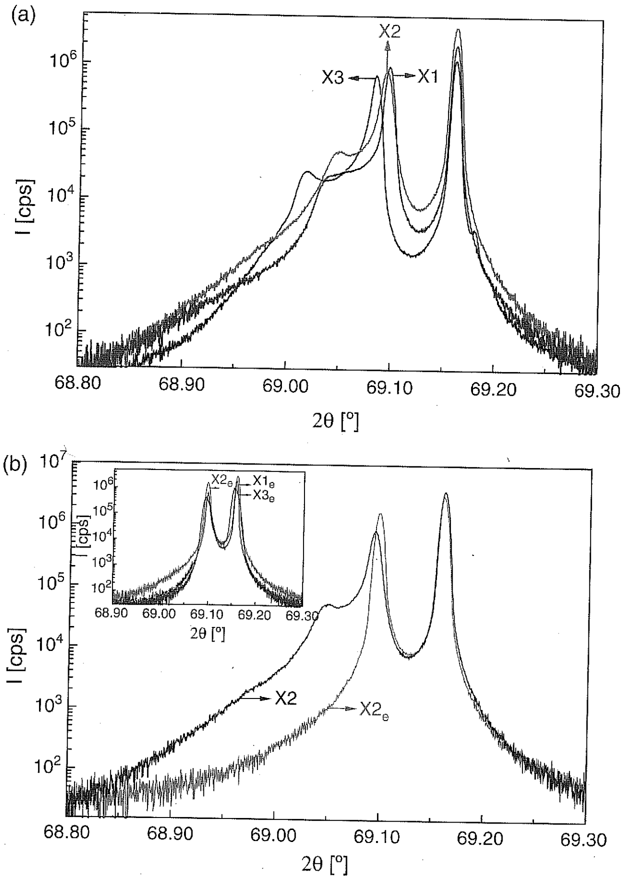

Fig. 4. High resolution XRD rocking curves acquired for: (a) initial PS layers (Xi); (b) X2 sample before and after the additional etching process—insert with XRD patterns for Xi$_e$ samples.

The HR-XRD patterns obtained for the initial samples—Figure 4(a)—show the presence of at least two Bragg peaks, where: the narrow peak at higher diffraction angle, around 69.16°, is typical for highly doped Si–p substrate,[26, 27] and respectively, the peaks at the lower diffraction angle, in the range 69°–69.10°, originate from PS film. From the spectra deconvolution in this domain, a shoulder is clearly observed in PS diffraction region towards lower values being an indication of the presence of two layers with different strain profiles; while the main peak is characteristic for bulk-PS layer, this shoulder indicates that a superficial layer, with a higher strain is formed at the surface of samples, resulting from the structural relaxation of bulk PS plastic deformation.

Moreover, "the logical evolution" does not apply in the case of X3 sample; this sample is the most strained one, the strain being so high that another surface layer (highly compressed one) is formed to compensate it leading to a new peak at 69.18 degrees. Further increase in the current will produce the amorphisation of this surface layer. The PS surface layer is in a highly extension state, the lattice spacing being higher than that of the bulk silicon layer, because of material left into the pores after pore formation process step.

The lower diffraction angle of PS peaks shows that the interplanar distances increase along [100] direction and consequently the layer suffers a tensile stress, validating the Raman results. From the angular separation $\Delta\theta$ between film and substrate peaks, the lattice mismatch or the strain $\Delta d/d$ normal to the interface has been calculated by using Bragg's equation in its differential form: $\Delta d/d = -\Delta\theta/tg\theta_B$ (θ_B being the Bragg diffraction angle); the values are presented in Table II, and it could be observed the linear correlation between porosity and strain, which is consistent with the previous reports.[28] On the other hand, for each type of PS film the strain value for bulk layer is approximately two times lower than those of surface layer.

Furthermore, the additional etching process leads to simplification of XRD patterns where low diffraction angle shoulders disappear, as shown in Figure 4(b). Regarding the other peaks, corresponding to the substrate and the bulk-PS layer, their positions are approximately unchanged, indicating that the highly stressed top PS layer has been etched. Regarding the origin of this layer, from θ–2θ diffraction scan we can only assume that the low angle shoulder came from relaxation of bulk PS plastic deformation. In this case, for partially relaxed structures, the single rocking curve measurement is not sufficient, being necessary also to differentiate between changes in lattice plane spacing to change in orientation of the lattice plane.

In order to eliminate and separate peak contributions of the individual layers, we performed for each of our samples several RSM, both symmetric, skew symmetric and asymmetric ultrahigh resolution set-up (grazing incidence and/or grazing exit asymmetric RSM). This technique allows also clearly and unambiguously determination the origin and effect of process induced strain on our porous silicon samples and we have used the absolute ultra high resolution multiple reflection multiple crystal XRD method (UHRMRMC–XRD, 4 reflection incident beam/monochromator, 1 reflection on the sample and 2 at the detector/analyzer) and we have also performed reciprocal space maps (both symmetric and asymmetric) on each of our samples, in the same experimental set-up.

Triple axis reciprocal space mapping (RSM) technique allows systematically variation of the angle of incidence and the diffraction angle allows displaying of the diffraction intensity data in a two-dimensional X-ray diffraction intensity map that can be interpreted as a reciprocal space map of the reciprocal lattice points.[29] In this way, it has become possible to visualize the different contributions to the diffraction intensity map[30] and finding the correspondence of the low angle peak shoulder.

In Figure 5 there are presented symmetric RSMs recorded around the symmetric (004) Si reciprocal space points with grazing exit geometry for sample X2 before (a) and after (b) the additional etching process. The maps are plotted in reciprocal space coordinates Q_y parallel to

Table II. Internal strain distribution in PS layers.

Samples	Substrate Si(004)	PS_{bulk}	PS_{surf}	$(\Delta d/d)_{bulk}$ $[\times 10^{-3}]$	$(\Delta d/d)_{surf}$ $[\times 10^{-3}]$
X1	69.1596	69.0961	69.0446	0.8047	1.4591
X2	69.1604	69.0937	69.0453	0.8449	1.5433
X3	69.1602	69.0834	69.0175	0.9733	1.8098

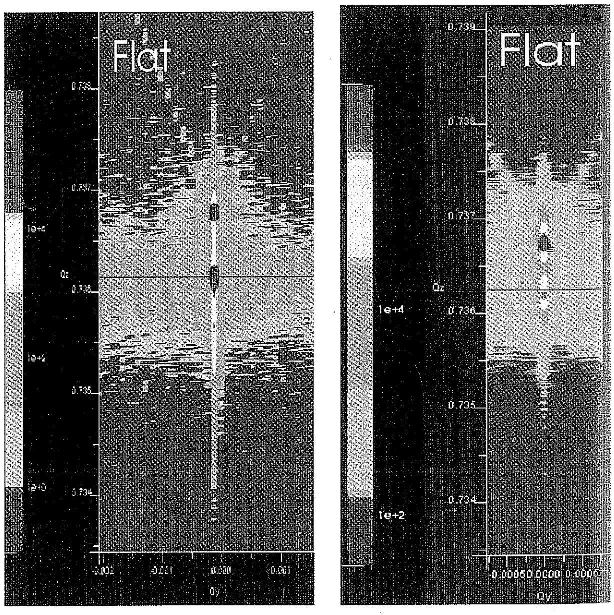

(a) (b)

Fig. 5. Symmetric RSM Si(004) for X2 sample before (a) and after (b) the additional etching process.

the sample surface and Q_z perpendicular to the sample surface. It could be observed that initial the sample map exhibits intense Bragg peaks coming from the unstrained Si substrate and respectively from PS bulk-layer, and also an area elongated in qz direction indicating some degree of lattice parameter variation along the $\langle 001 \rangle$ direction. These results revealed that porosification gave rise to a nonuniform strain distribution in the silicon substrate through the PS layer. In addition, while in Figure 5(a) a less intense peak is present, assigned to PS top-layer, in Figure 5(b) it disappears and furthermore the X-ray scattering is less diffuse.

Supplementary information about the PS top layer, and furthermore about the whole film internal structure, have been obtained using asymmetric (224) grazing exit for X3 sample before the additional etching process. This configuration eliminates effect of tilt and is very sensitive to local strain ($<10^{-4}$).[31] In Figure 6 it could be observed that there are four distinct areas on the map: the substrate peak, two intense peaks with different constant strain values and a wide area arising from the graded strain layer, already observed in the symmetric map. The pole figures demonstrate that the inter-atomic spacing is different in surface layer than in bulk layer,[32,33] and furthermore the presence of lattice deformation gradient in PS layer depth.

All of RSMs clearly demonstrate the presence of a surface PS layer, which is highly strained *This layer is not an oxide layer, it is a PS layer with a different microstructure*, removed after a short dip in HF, as it could be seen in both high resolution diffraction scans and RSMs (symmetric and asymmetric).

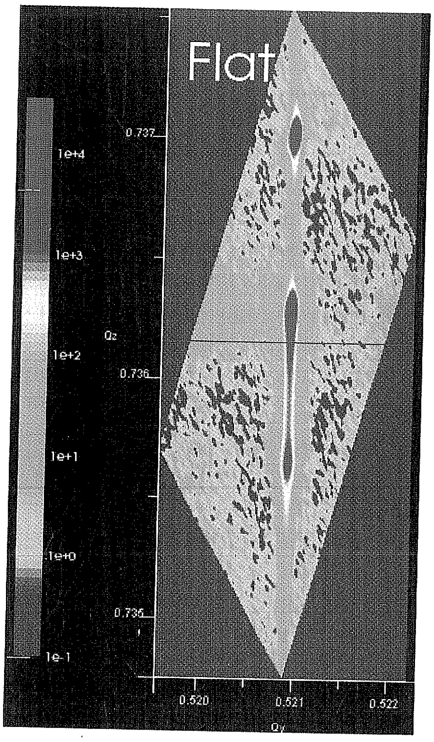

Fig. 6. Asymmetric (224) grazing exit for X3 sample before the additional etching process.

4. CONCLUSIONS

The nanostructure of porous layers obtained on highly doped p^+ type Si substrate (1–5 $m\Omega \cdot cm$) was investigated via FE-SEM, Raman scattering and SAXS. While the morphological analyses show that the average pore diameter, as well as the film thickness increase with increasing applied current, the spectrometric techniques reveal the corresponding diminish of crystallite size. On the other hand, the Raman spectra present features which might have different causes, and in order to have a correct understanding, to differentiate between the quantum effects, internal strain and chemical composition, advanced XRD methods have been used. It has been demonstrated that position and broadening of the Raman peaks corresponding to nanostructurated layer have to be corrected taking into account the particularity of silicon porosification process, specifically formation during the PS advancement of a superficial layer. Furthermore, symmetrical and asymmetrical rocking curves obtained by high-resolution X-ray diffraction completed with reciprocal space maps (RSMs) support our approach, being clearly shown that the PS film in-depth contains two layers—bulk and highly strained superficial layer, with a graded strain inter-layer. In the same time, for advanced MEMS applications, it has been demonstrated that an additional etching process is necessary, being adequate to eliminate the highly strain PS top-layer and to improve the quality of complex devices.

Acknowledgments: M. Miu acknowledges that the research presented in this paper is supported by the Sectoral Operational Programme Human Resources Development (SOP HRD), financed from European Social Fund and by the Romanian Government under the contract number *POSDRU/89/1.5/S/63700*. This work was also partially supported by the PN II–IDEI program under ID-883 project. The authors are grateful to Phys. A. Dinescu for help with the SEM observations and Eng. F. Comanescu and Dr. M. Purica for the Raman spectroscopy measurements.

References and Notes

1. J. Kanungo, H. Saha, and S. Basu, *Sens. Actuator B* 140, 65 (**2009**).
2. V. Torres-Costa, F. Agullo-Rueda, R. J. Martín-Palma, and J. M. Martínez-Duart, *Opt. Mater.* 27, 1084 (**2005**).
3. D. Song, N. Tokranova, A. Gracias, and J. Castracane, *J. Micro/Nanolith. MEMS, MOEMS* 7, 021013 (**2008**).
4. M. Miu, A. Angelescu, I. Kleps, S. Petrescu, L. Zdrentu, M. Simion, and T. Ignat, *Phys. Stat. Sol. (c)* 4, 2093 (**2007**).
5. A. Gajovic, D. Gracin, I. Djerdj, N. Tomasic, K. Juraic, and D. S. Su, *Appl. Surf. Sci.* 254, 2748 (**2008**).
6. D. Han, J. D. Lorentzen, J. Weinberg-Wolf, L. E. McNeil, and Q. Wang, *J. Appl. Phys.* 94, 2930 (**2003**).

7. I. De Wolf, *Semicond. Sci. Technol.* 11, 139 (**1996**).
8. Q. Li, W. Qiu, H. Tan, J. Guo, and Y. Kang, *Optics and Lasers in Engineering* 48, 1119 (**2010**).
9. D. K. Bowen and B. K. Tanner, High Resolution X-ray Diffractometry and Topography, Taylor & Francis, London (**1998**).
10. V. G. Kravets and V. Yu, *Kolmykova, Optics and Spectroscopy* 99, 68 (**2005**).
11. S. Piscanec, A. C. Ferrari, J. A. Zapien, Y. Lifshift, S. T. Lee, S. Hofmann, and J. Robertson, *Phys. Rev. B* 68, 241312(R) (**2003**).
12. R. Kumar and A. K. Shukla, *Phys. Lett. A* 373, 2882 (**2009**).
13. R. Tsu, H. Shen, and M. Dutta, *Appl. Phys. Lett.* 60, 112 (**1992**).
14. C. Tsai, K. H. Li, J. Sarathy, S. Shih, J. C. Campbell, B. K. Hance, and J. M. White, *Appl. Phys. Lett.* 59, 2814 (**1991**).
15. Y. A. Pusep, A. D. Rodrigues, J. C. Galzerani, R. D. Arce, R. R. Koropecki, and D. Comedi, *J. Electrochem. Soc.* 156, K215 (**2009**).
16. B. Li, D. Yu, and S.-L. Zhang, *Phys. Rev. B* 59, 1645 (**1999**).
17. X. G. Zhang, *J. Electrochem. Soc.* 151, C69 (**2004**).
18. I. H. Campbell and P. M. Fauchet, *Sol. Stat. Commun.* 58, 739 (**1986**).
19. H. Richter, Z. P. Wang, and L. Ley, *Sol. Stat. Commun.* 39, 625 (**1981**).
20. F. Cerdeira and M. Cardona, *Phys. Rev. B* 5, 1440 (**1972**).
21. G. Renaud, R. Lazzari, and F. Leroy, *Surf. Sci. Rep.* 64, 255 (**2009**).
22. A. Gril, V. Patel, K. P. Rodbell, E. Huang, M. R. Baklanov, K. P. Mogilnikov, M. Toney, and H.-C. Kim, *J. Appl. Phys.* 94, 3427 (**2003**).
23. M. Miu, M. Danila, T. Ignat, I. Kleps, F. Craciunoiu, M. Simion, A. Bragaru, and A. Dinescu, *Superlattices Microstruct.* 46, 291 (**2009**).
24. A. B. Horsfall, J. M. M. dos Santos, S. M. Soare, N. G. Wright, A. G. O'Neill, S. J. Bull, A. J. Walton, A. M. Gundlach, and J. T. M. Stevenson, *Semicond. Sci. Technol.* 18, 992 (**2003**).
25. W. Wei, *Wacuum* 81, 857 (**2007**).
26. G. Bhagavannarayana, S. N. Sharma, R. K. Sharma, and S. T. Lakshmikumar, *Mater. Chem. Phys.* 97, 442 (**2006**).
27. I. M. Young, M. I. J. Beale, and J. D. Benjamin, *Appl. Phys. Lett.* 46, 1133 (**1985**).
28. C. S. Solanki, R. R. Bilyalov, J. Poortmans, G. Beaucarne, K. V. an Nieuwenhuysen, J. Nijs, and R. Mertens, *Thin Solid Films* 451–452, 649 (**2004**).
29. G. V. Hansson, H. H. Radamsson, and W.-X. Ni, *J. Mater. Sci. Mater Electron* 6, 292 (**1995**).
30. E. Abramov, A. F. Beloto, M. Ueda, R. Gunzel, and H. Reuther, *Nucl. Instr. Meth. Phys. Res. B* 175–177, 229 (**2001**).
31. T. Baumbach, D. Lubbert, and M. Gailhanou, *J. Appl. Phys.* 87, 3744 (**2000**).
32. M. Y. Ghannam, M. M. Hassan, V. DePauw, G. Beaucarne, J. Poortmans, and R. Mertens, *Thin Solid Films* 516, 6924 (**2008**).
33. L. Pascual, R. J. Martin-Palma, A. R. Landa-Canovas, P. Herrero, and J. M. Martinez-Duart, *Appl. Phys. Lett.* 87, 251921 (**2005**).

Received: 15 January 2010. Accepted: 1 April 2010.